November 1, 2001

Climatology of mid- and low-latitude F region disturbance winds measured by WINDII

J. T. Emmert
Bela G. Fejer, *Utah State University*
C. G. Fesen
G. G. Shepherd
B. H. Solheim

JOURNAL OF GEOPHYSICAL RESEARCH, VOL. 106, NO. A11, PAGES 24,701-24,712, NOVEMBER 1, 2001

Climatology of middle- and low-latitude daytime *F* region disturbance neutral winds measured by Wind Imaging Interferometer (WINDII)

J. T. Emmert and B. G. Fejer

Center for Atmospheric and Space Sciences, Utah State University, Logan, Utah

C. G. Fesen

W. B. Hanson Center for Space Sciences, University of Texas at Dallas, Richardson, Texas

G. G. Shepherd and B. H. Solheim

Centre for Research in Earth and Space Science, York University, Toronto, Ontario, Canada

Abstract. We have modeled the global climatology of middle- and low-latitude *F* region daytime disturbance neutral winds using extensive measurements by the Wind Imaging Interferometer (WINDII) instrument on board the UARS. The perturbation winds were obtained by subtracting the quiet time values from the disturbed winds along the satellite orbit, which effectively removes average measurement bias. The zonal disturbance winds are mostly westward (except in the early morning sector), increase with latitude, and have largest values in the late afternoon sector. In general, the meridional perturbation winds are equatorward, increase linearly with latitude, and decrease from early morning to afternoon hours. The zonal and meridional perturbations increase roughly linearly with *Kp* and expand to lower latitudes with increasing magnetic activity. The meridional disturbance winds are largest for low solar flux conditions. We present empirical analytical models for longitudinally averaged disturbance winds from 60° to the equator. Our model winds are in poor agreement with results from the empirical wind model Horizontal Wind Model-93 during the entire daytime period. There are also important discrepancies between the average perturbations winds from WINDII and the National Center for Atmospheric Research thermosphere-ionosphere electrodynamic general circulation model, particularly at midlatitudes. These differences could be explained in part by the storm time dependence of the disturbance winds and by the variability of the high-latitude electric fields.

1. Introduction

Over the past 3 decades, ground-based and satellite measurements and model studies have been used to determine the quiet time diurnal, seasonal, and solar cycle variations of the middle- and low-latitude *F* region neutral winds [e.g., *Hernandez et al.*, 1980; *Hagan*, 1993; *Titheridge*, 1995; *Miller et al.*, 1997]. There have also been numerous experimental and theoretical studies of thermospheric winds during disturbed conditions [e.g., *Hernandez*, 1982; *Roble et al.*, 1987; *Crowley et al.*, 1989; *Miller et al.*, 1990; *Duboin and Lafeuille*, 1992; *Fesen et al.*, 1993, 1995; *Fuller-Rowell et al.*, 1994, 1996; *Buonsanto*, 1995; *Burns et al.*, 1995; *Fujiwara et al.*, 1996; *Emery et al.*, 1996], but these have not focused on the average response of daytime global winds to magnetic activity. Recently, *Buonsanto and Witasse* [1999] studied the climatology of meridional winds derived from Millstone Hill (42.6°N, 288.5°E) radar data. They reported significant magnetic activity effects on the meridional winds only during solar minimum summer conditions. *Kawamura et al.* [2000] discussed the morphology of thermospheric winds in the magnetic meridional plane measured by the Shigaraki (34.9°N, 131.1°E) middle and upper atmosphere radar. *Kawamura et al.* reported a strongly equatorward DC component for high magnetic activity, but they did not examine magnetic activity effects in detail.

The Wind Imaging Interferometer (WINDII) instrument on board the UARS satellite has made extensive measurements of thermospheric winds. Most of the earlier studies using this database have focused on the dynamics of the lower thermosphere. Recently, *Fejer et al.* [2000] presented initial results of middle- and low-latitude daytime *F* region average disturbance winds (the mean change in the winds during geomagnetically disturbed periods) derived from WINDII data. They showed that the average disturbance winds change significantly from morning to afternoon, are largely independent of season, and increase approximately linearly with the *Kp* index. They also showed that there is very good agreement between the zonal disturbance winds from WINDII and from the wind and temperature spectrometer on board the DE-2 satellite. *Zhang and Shepherd* [2000] presented the first

Paper number 2000JA000372
0148-0227/01/2000JA000372$09.00

case study of thermospheric winds measured by WINDII between 90 and 200 km during a large magnetic storm and showed storm-induced winds penetrating down to altitudes of about 120 km.

In this work, we present the climatology of the middle- and low-latitude *F* region daytime disturbance winds using a very large database of WINDII measurements. In the following sections, we first briefly describe the WINDII database and our method of calculating disturbance winds. Then, we examine the main characteristics of these disturbance winds and derive empirical analytical models of their longitudinally averaged climatology. Finally, we compare our model results with those from global circulation models.

2. Data and Methodology

The UARS is in a nearly circular, 57° inclination orbit, at a height of 585 km. The orbital period is 96 min, and the precession rate is 5° d^{-1}, so that all local times are sampled every 36 days. The UARS mission was described in detail by *Reber et al.* [1993].

WINDII is a limb-scanning Michelson interferometer that views latitudes from 42°S to 42°N continuously, and up to 72° in alternating hemispheres, as the satellite executes a 180° yaw maneuver every 36 days [*Shepherd et al.*, 1993]. In general, WINDII measures both the 557.0 nm O^1S (green line) and 630.0 nm O^1D (red line) airglow emissions over the 90-300 km altitudinal range during the day, with height resolutions of 3 km below 120 km and 5 km at higher altitudes. The temporal resolution is about 30 s, which corresponds to a latitude resolution of about 2° at the equator. *F* region nighttime data consist only of red line measurements, which are made only 1 day per week. Horizontal vector winds are derived from line-of-sight wind measurements at the Earth's limb at 45° and 135° from the satellite's forward direction. These two fields of view sample the same volume within about 8 min of each other. The uncertainty of a single measurement of the wind velocity near 250 km is about 40 m s^{-1} for the green line data and 20 m s^{-1} for the red line data.

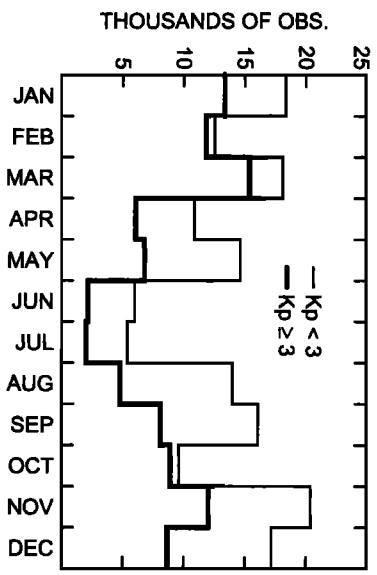

Figure 1. Monthly distribution of WINDII thermospheric wind measurements used in the present study.

Our database consists of ~300,000 height profiles of the horizontal wind velocity in the 125-300 km altitudinal range, obtained on about 600 days from November 1991 through August 1996; the average decimetric solar flux index is about 125. This database is slightly larger than that used by *Fejer et al.* [2000], which consisted of 295,000 height profiles and had an average decimetric solar flux index of 126. Figure 1 presents the monthly distribution of observations at 250 km under quiet ($Kp < 3$) and disturbed ($Kp \geq 3$) conditions. December solstice months contain the largest number of measurements, and June solstice months contain the smallest. High solar activity data, gathered only during the early part of the mission, is mostly from December solstice and equinox periods.

We study magnetic activity-driven daytime *F* region disturbance winds at latitudes below 60°, using measurements in the 225-275 km height range. In our earlier study, the disturbance winds were determined using measurements only in the 240-260 km height range, but as we will see later, the perturbations winds do not change much with altitude. As described by *Fejer et al.* [2000], we analyze the characteristics of perturbation winds obtained by removing average quiet time effects [e.g., *Fejer and Scherliess*, 1995, 1997]. We defined magnetically quiet periods by $Kp < 3$ (average $Kp \equiv 1.7$), and we determined quiet time reference averages by averaging the wind data along the orbit of the satellite, treating red and green line measurements separately. The observed winds are located 15° from the satellite's track and on alternating sides because of the spacecraft's yaw maneuvers. These two configurations (north looking and south looking) correspond to different local time-latitude conditions, so we treated the associated data separately.

The use of orbital coordinates ensures more even sampling than local time-latitude bins, which tend to collect more data near the orbital turnaround points than elsewhere. More importantly, it provides a straightforward way of removing, from the disturbance winds, average measurement bias, as described below. Wind measurements from ascending (south-to-north) and descending (north-to-south) orbits may differ by as much as 50-75 m s^{-1} (at 250 km) for identical geophysical conditions; similar differences occur between north looking and south looking observations. The possible causes of these differences are under investigation.

We initially calculated quiet time reference averages for each 5 km height level using three seasonal bins: December solstice (November-February), June solstice (May-August), and combined equinoxes (March-April and September-October). We also applied small solar flux and longitude corrections. Our quiet time reference averages (which depend on the observing geometry) and corrections are described in more detail by *Emmert* [2001]. Work on our quiet time models is still in progress; therefore we do not present the models here.

We calculated residual winds by arranging all disturbed ($Kp \geq 3$) wind measurements in the same bins used for the quiet time averages and then subtracting from each measurement the corresponding quiet time mean value. These perturbations contain storm time-dependent magnetic activity effects that also vary with local time, latitude, solar activity, season, and longitude. In addition, they contain variability due to short-term (min to days) processes and residual instrumental effects. For the results described here we averaged the residual winds over the 225-275 km height range; our data are largely independent of height above 150 km. We use a broader height

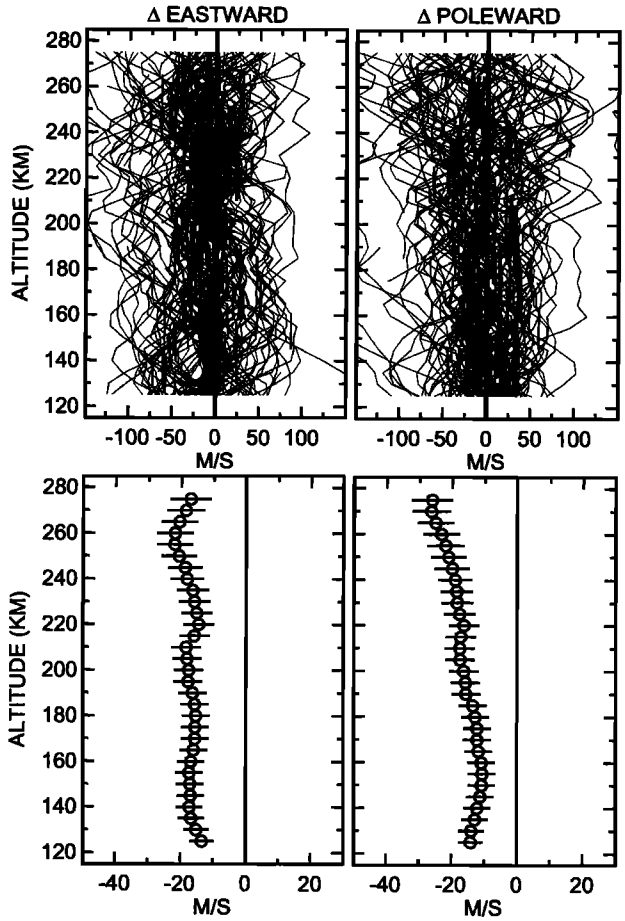

Figure 2. (top) Scatterplots of height profiles of early morning midlatitude disturbance winds derived from WINDII observations (ΔKp =2.5, 0500-0900 LT, and 30°-40°N). (left) Change eastwards. (right) Change poleward. (bottom) Average disturbance winds as a function of height for the same conditions. The horizontal bars indicate the estimated standard errors of the mean.

range than in our initial results [*Fejer et al.*, 2000] since this helps to reduce the noise in the green line data.

We grouped the residuals by the associated 3 hour *Kp* indices and calculated the corresponding average perturbations, standard deviations, and standard errors of the mean. We obtained our standard errors of the mean by dividing the standard deviations by the square root of the number of independent days (instead of the number of observations). This is a more stringent and, we believe, a more realistic measure since satellite data from a given pass are correlated.

The above procedure effectively removes from the average perturbation winds most of the average instrument bias, reducing it to <10 m s^{-1}. Finally, we analyzed the characteristics of the average wind perturbations as a function of local time, season, solar flux, latitude, and magnetic activity. The disturbance wind results presented in the following sections correspond to longitudinally averaged conditions.

3. Results

In this section, we first briefly examine the general characteristics of the disturbance winds. Then, we present local time-, latitude-, season-, and solar flux-dependent empirical models of longitudinally averaged disturbance winds as a function of the *Kp* index.

3.1. General Characteristics of the WINDII Average Disturbance Winds

Figure 2 (top) presents typical scatterplots of early morning midlatitude zonal and meridional disturbance winds ($Kp > 3$) as a function of height. This bin contains about 3000 height profiles, but for clarity, only a random sample of 100 is shown. Figure 2 (bottom) shows height profiles of the average perturbation winds from the full data sample; the error bars indicate the estimated standard errors of the mean. The disturbance winds are slightly larger at higher altitudes but do not change much with height above about 150 km; data from other local times and latitudes give similar results. In this paper, we use wind residuals averaged over the 225-275 km height range.

Fejer et al. [2000] pointed out that the WINDII disturbance wind latitudinal patterns do not change much with season and are nearly identical in the Northern and Southern Hemispheres. Figure 3 shows seasonally averaged zonal and meridional disturbance winds at six latitudinal sectors as a function of solar local time. The data with the error bars were obtained by averaging the residuals from both the Northern and Southern Hemispheres in 3 hour overlapping bins at 1.5 hour intervals; the error bars are the estimated standard errors of the mean. The smooth curves represent the results from an analytical empirical model, to be described later. Figure 3 indicates that meridional (zonal) disturbance winds are largest in the

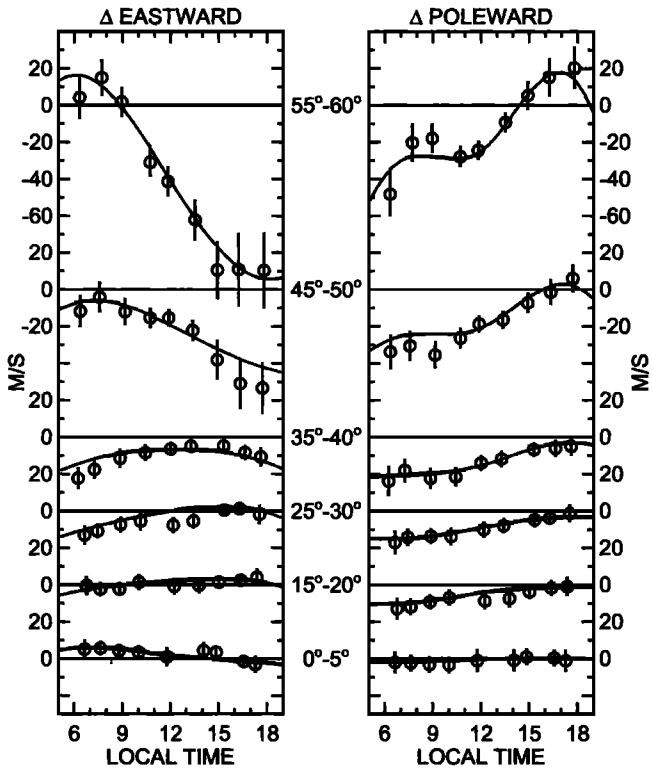

Figure 3. Local time variations of the seasonally averaged WINDII disturbance winds (ΔKp = 2.5): (left) change eastward and (right) change poleward. The vertical bars denote the estimated standard errors of the mean.

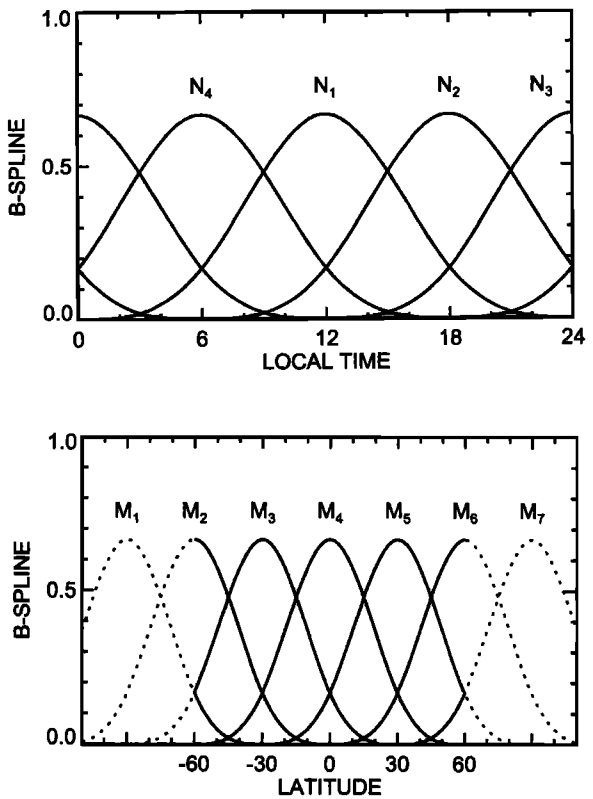

Figure 4. Cubic B splines used to represent the local time and latitude variation of the disturbance winds.

morning (afternoon) sector and decrease toward the equator [*Fejer et al.*, 2000].

The results presented above were obtained by combining data from all longitudes and solar flux values. Recall that we accounted for quiet time solar flux effects in our reference averages using an empirical correction; any remaining solar activity dependence in the average disturbance winds is therefore associated with disturbed conditions. We examined solar flux effects by comparing the latitudinal profiles of the disturbance winds for average decimetric solar flux indices of 90 and 150. The meridional disturbance winds show consistently larger equatorward perturbations in the lower solar flux case. The zonal wind data have slightly larger (about 10 m s^{-1}) westward perturbations before 0900 LT in the lower solar flux case but are essentially independent of flux at later local times. In section 3.2, we introduce a small empirical solar flux-dependent correction to our meridional disturbance winds; the zonal perturbation winds will be assumed to be independent of solar activity.

We also briefly investigated the importance of longitudinal effects by comparing the latitudinal profiles from the eastern (30°W-180°E) and western (180°-30°W) sectors, where the magnetic dip equator is north and south, respectively, of the geographic equator. In general, the data suggest a complex longitudinal dependence, although there is a tendency for the latitudinal patterns to be centered on the magnetic dip equator, especially for the morning zonal winds. In addition, as expected, auroral zone effects occur at lower northern (southern) geographic latitudes in the western (eastern) sector. The longitude dependence of the meridional perturbation winds is less clear. These effects will not be discussed further here.

3.2. Average Disturbance Wind Models

Our database is not extensive enough for the development of an empirical model that fully accounts for seasonal, solar cycle, and magnetic activity effects in both the Northern and Southern Hemispheres; we therefore constructed two models. The first one, obtained by averaging the perturbation winds from all seasons, longitudes, and Northern and Southern Hemispheres, describes the dependence of the perturbation winds on local time, latitude, and magnetic activity. In this case, we have also incorporated a relatively simple solar flux correction for the meridional winds. Our second model describes, for each season, the local time-latitude variations of the longitudinally averaged disturbance winds from 60°S to 60°N, but only for an average $\Delta Kp = 2.5$. Although both of these models were derived from measurements between 225 and 275 km, they should provide a fairly realistic representation of the disturbance winds down to altitudes of about 150 km. It is important to note, however, that they do not account for the variability resulting from time-dependent storm effects.

3.2.1. *Kp*-dependent disturbance wind model. We calculated our seasonally averaged disturbance wind model by performing a least squares fit of the wind residuals. These perturbation winds were modeled as

$$U_d(t,\theta,\Delta Kp) = \sum_{i=1}^{4}\sum_{j=0}^{3}\sum_{k=1}^{2} a_{ijk} N_i(t)(\theta/10)^j(\Delta Kp)^k \quad (1)$$

$$V_d(t,\theta,\Delta Kp) = \sum_{i=1}^{4}\sum_{j=1}^{3}\sum_{k=1}^{2} b_{ijk} N_i(t)(\theta/10)^j(\Delta Kp)^k, \quad (2)$$

where U_d and V_d are the zonal and meridional daytime perturbation winds, respectively, in m s^{-1}, t denotes solar local time, θ = |geographic latitude|, and $\Delta Kp = Kp - 1.7$, with negative values set to zero. $N_i(t)$ are the normalized cubic splines in local time shown in Figure 4 (top). These functions have nodes at 0, 6, 12, and 18 hours; nighttime measurements were included in the fit to stabilize the model at dawn and dusk. This WINDII model is valid for 0500-1900 LT, for latitudes up to 60°, and for Kp values up to about 7. The model coefficients a_{ijk} and b_{ijk} are given in Tables 1 and 2; note that the $j = 1$ terms are not used for the zonal component since they do not improve the quality of the fit.

Table 1. Seasonally Averaged Disturbance Wind Model Coefficients a_{ijk} for the Zonal Component

	$i=1$	$i=2$	$i=3$	$i=4$
		k = 1		
$j=0$	-1.49E-02[a]	1.48E+00	4.38E-01	6.58E+00
$j=1$	0.00E+00	0.00E+00	0.00E+00	0.00E+00
$j=2$	-8.63E-01	4.77E+00	-4.82E+00	-1.00E+00
$j=3$	1.67E-01	-1.15E+00	1.18E+00	6.11E-02
		k = 2		
$j=0$	3.50E-01	-1.33E+00	-1.57E+00	-9.22E-01
$j=1$	0.00E+00	0.00E+00	0.00E+00	0.00E+00
$j=2$	5.33E-01	-1.02E+00	1.08E+00	-6.29E-01
$j=3$	-1.32E-01	2.00E-01	-3.23E-01	1.76E-01

[a]Read -1.49 E-02 as -1.49×10^{-2}.

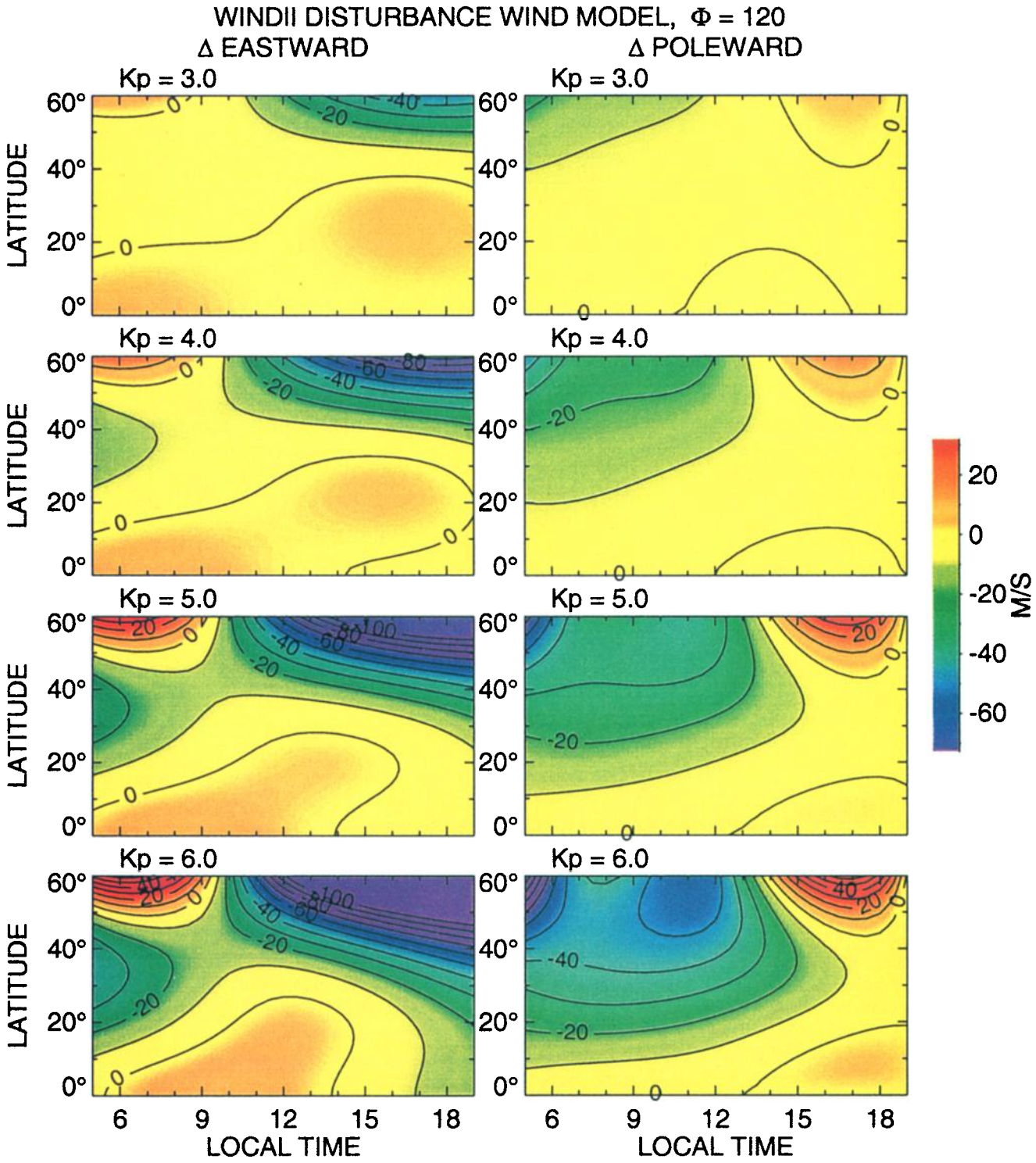

Plate 1. Seasonally averaged zonal and meridional WINDII model winds at various magnetic activity levels.

Table 2. Seasonally Averaged Disturbance Wind Model Coefficients b_{ijk} for the Meridional Component

	$i=1$	$i=2$	$i=3$	$i=4$
		$k=1$		
$j=1$	2.21E+00	-2.31E-01	1.09E+00	-3.23E+00
$j=2$	-1.11E+00	8.46E-01	-2.62E+00	1.47E+00
$j=3$	1.39E-01	-1.67E-01	5.14E-01	-2.70E-01
		$k=2$		
$j=1$	-1.45E+00	2.02E+00	-2.88E+00	5.58E-01
$j=2$	5.13E-01	-1.52E+00	2.60E+00	-7.84E-01
$j=3$	-8.96E-02	2.70E-01	-5.24E-01	1.61E-01

This model describes the disturbance winds for an average $F_{10.7}$ solar flux index $\Phi \cong 120$. As mentioned earlier, the daytime zonal disturbance winds are largely independent of solar flux, but the meridional perturbations, which are mostly equatorward, increase with decreasing solar activity. We calculated a simple solar flux correction term for the meridional winds by first subtracting from each original (solar flux dependent) meridional wind perturbation the corresponding wind value calculated from our flux-independent model. Figure 5 shows the solar flux dependence of these second-order residuals for daytime midlatitude (30°-60°) conditions. Then, using an idealized bilinear solar flux dependence, we performed a least squares fit of all second-order daytime residuals to obtain the following (latitude- and Kp-dependent), solar flux correction term:

$$V_{cor}(\Phi,\theta,\Delta Kp)=1.72\times10^{-3}(\Psi-115)(\theta)(\Delta Kp), \quad (3)$$

where $\Psi = \Phi$, the $F_{10.7}$ index, for $\Phi < 150$, and $\Psi = 150$ for higher flux values. The solid lines in Figure 5 show this term evaluated at 45° latitude and for $\Delta Kp = 2.5$. Although this correction is not rigorous, it provides a reasonable estimate of solar flux effects. The flux-corrected meridional wind perturbations are then given by $V_{dcor}(t,\theta,\Delta Kp,\Phi)=V_d+V_{cor}$.

Plate 1 illustrates the local time and latitudinal variations of the model disturbance winds for $\Phi = 120$ and different magnetic activity levels. Plate 1 indicates that the zonal perturbations are westward at midlatitudes and eastward at high and equatorial latitudes before 0900 LT and that they become increasingly westward above 30° at later local times. The meridional perturbations are equatorward before about 1400 LT; later, they become slightly poleward at upper midlatitudes. The disturbance winds increase nearly linearly with magnetic activity, but in the early morning and late afternoon they also expand to lower latitudes. Since our disturbance winds are longitudinally averaged in geographic coordinates, under strongly disturbed conditions they should be affected, via ion drag, by enhanced ionospheric convection down to latitudes of about 45°-50° near dawn and dusk. This is consistent with precipitating electron data from Defense Meteorological Satellite Program, which showed that for $Kp = 5$ the equatorward edge of the diffuse aurora extends down to magnetic latitudes of 58° near dawn and 64° in the late afternoon sector [*Gussenhoven et al*, 1983]. Studies of DE-2 zonal winds and ion drifts during very disturbed periods showed convection-driven winds at magnetic latitudes as low as 35° [*Reddy and Mayr*, 1998].

3.2.2. Season-dependent disturbance wind model. We developed season-dependent disturbance wind models by performing a least squares fit of the residuals as a function of local time and latitude (but not Kp). In this case the local time dependence was again accounted for by the cubic splines shown in Figure 4 (top), while the latitudinal dependence was represented by seven cubic splines with nodes spaced by 30° (Figure 4 (bottom)). The resulting models may be written as

$$U_d(t,\theta)=\sum_{i=1}^{4}\sum_{j=1}^{7}c_{ij}N_i(t)M_j(\theta) \quad (4)$$

$$V_d(t,\theta)=\sum_{i=1}^{4}\sum_{j=1}^{7}d_{ij}N_i(t)M_j(\theta), \quad (5)$$

where U_d and V_d are the zonal and meridional daytime, season-dependent perturbation winds, respectively, in m s^{-1}, t denotes solar local time, θ = geographic latitude, and $N_i(t)$, $M_j(\theta)$ are the cubic splines in local time and latitude, respectively, shown in Figure 4. A disturbed condition of $Kp > 3$ was used to select residuals for the fit; the resulting models represent an average Kp of 4.2. These models are valid for daytime local times and latitudes up to 60°. The model coefficients c_{ij} and d_{ij} are given in Tables 3 and 4 for each season. The results from these models will be presented in section 4.

4. Comparison With Results From Global Wind Models

The Horizontal Wind Model (HWM) [*Hedin et al.*, 1988, 1991, 1996] integrates wind data from ground-based and spaced-based instruments into a single global model. The input parameters are geographic location, local time, altitude, season, solar activity, and magnetic activity. Data gaps are covered by interpolation using both empirical and physically based basis functions. The magnetic activity parameterization in the HWM is similar to that used in the Mass Spectrometer Incoherent Scatter model [*Hedin et al.*, 1987] and has only weak local time and seasonal dependence.

Figure 6 presents the local time-latitude vector disturbance winds from our seasonally averaged WINDII model and from the HWM-93, both for $\Delta Kp = 3$. The HWM-93 disturbance

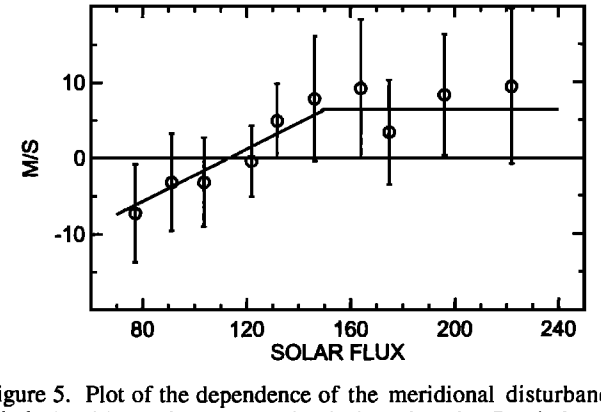

Figure 5. Plot of the dependence of the meridional disturbance winds (positive poleward) on the decimetric solar flux index.

Table 3. Seasonally Dependent Disturbance Wind Model Coefficients c_{ij} for the Zonal Component

	$j=1$	$j=2$	$j=3$	$j=4$	$j=5$	$j=6$	$j=7$
				December Solstice			
$i=1$	-2.25E+02	-4.10E+01	-9.13E+00	1.59E+01	-6.19E+00	5.52E-01	8.56E+01
$i=2$	-5.70E+02	-1.24E+02	5.97E+01	-3.15E+01	7.43E+00	-1.08E+02	-8.95E+02
$i=3$	-2.69E+02	1.14E+02	-6.04E+01	3.52E+00	-2.47E+01	-8.40E+01	2.30E+03
$i=4$	2.93E+02	3.68E+01	-4.55E+01	2.92E+01	-2.12E+01	6.61E+00	-6.24E+02
				June Solstice			
$i=1$	-9.41E+02	2.96E+00	5.29E+01	-9.25E-01	-4.36E+01	1.40E+02	-1.36E+03
$i=2$	3.24E+02	-1.96E+02	3.48E+01	-4.97E+01	1.18E+02	-3.19E+02	8.37E+02
$i=3$	8.53E+01	-2.86E+02	3.43E+01	-3.09E+01	-1.88E+02	4.54E+02	-5.40E+03
$i=4$	7.13E+02	3.32E+01	-7.71E+01	2.67E+01	9.98E+00	-1.68E+02	2.09E+03
				Equinox			
$i=1$	-2.16E+02	1.28E+01	-3.09E+01	2.43E+01	3.36E+00	3.22E+01	-5.42E+02
$i=2$	-1.09E+03	-1.23E+02	4.09E+01	-2.31E+01	3.77E+00	-2.02E+01	-3.98E+02
$i=3$	2.17E+03	-1.82E+02	-3.16E+00	-3.06E+01	5.33E+01	-3.08E+02	2.17E+03
$i=4$	1.12E+02	-2.88E+01	-2.90E+00	4.07E+01	-4.78E+01	-5.82E+01	6.90E+02

winds were obtained by first subtracting the quiet (Kp = 2) from the disturbed (Kp = 5) model results at a height of 250 km and for a solar flux index of 125, with seasonal and longitudinal effects disabled (i.e., corresponding to seasonally and longitudinally averaged winds), and then averaging the results from the Northern and Southern Hemispheres. Figure 6 shows largest WINDII perturbation winds at upper midlatitudes, where they are predominantly equatorward in the morning and westward in the afternoon. The HWM-93 wind patterns show mostly large westward disturbances at all local times and latitudes, even near the equator. Figure 7 shows comparisons of the latitudinal profiles of the disturbance winds from WINDII and HWM-93. The large westward disturbances predicted by the HWM-93 are again evident throughout the day at essentially all latitudes. Surprisingly, this model gives afternoon zonal wind perturbations winds with largest values at equatorial latitudes, which is inconsistent with our data. The mostly poleward

Table 4. Seasonally Dependent Disturbance Wind Model Coefficients d_{ij} for the Meridional Component

	$j=1$	$j=2$	$j=3$	$j=4$	$j=5$	$j=6$	$j=7$
				December Solstice			
$i=1$	-1.73E+02	1.13E+02	-1.99E+01	-1.71E+01	-2.59E+01	1.97E+01	-7.92E+02
$i=2$	-2.68E+02	-1.02E+02	3.87E+00	-1.59E+01	1.62E+00	-7.67E+01	1.39E+03
$i=3$	1.74E+03	1.21E+02	-3.22E+00	-1.42E+01	2.32E+00	3.22E+00	-1.46E+03
$i=4$	1.31E+01	-5.50E+01	5.23E+01	5.67E+00	2.47E+01	-1.77E+02	1.04E+03
				June Solstice			
$i=1$	-1.07E+03	1.34E+02	-3.80E+01	-5.21E+01	1.11E+02	-2.35E+02	7.23E+02
$i=2$	1.13E+03	-8.36E+01	3.73E+01	6.47E+01	-1.35E+02	2.25E+02	-6.94E+02
$i=3$	-2.35E+03	2.31E+02	1.26E+01	-6.59E+01	2.03E+02	-4.16E+02	2.08E+03
$i=4$	1.62E+03	-6.91E+01	6.57E+01	4.41E+01	-1.36E+02	1.54E+02	-9.12E+02
				Equinox			
$i=1$	-6.36E+01	-4.17E+00	4.10E+01	-2.98E+00	-4.82E+01	5.93E+01	-6.01E+02
$i=2$	-7.53E+01	5.43E+01	-1.79E+01	-6.94E-01	6.49E+01	-1.30E+02	1.21E+03
$i=3$	-6.55E+02	2.12E+01	2.44E+01	7.23E+00	-6.61E+01	4.56E+01	-6.42E+02
$i=4$	2.03E+01	1.20E+02	-4.60E+00	-1.13E+01	2.34E+01	-1.08E+02	4.81E+02

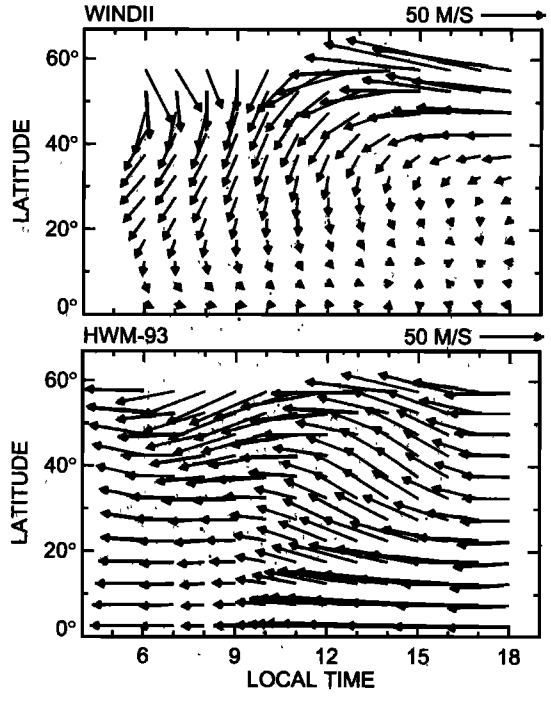

Figure 6. (top) WINDII and (bottom) HWM-93 seasonally and longitudinally averaged vector disturbance winds (ΔKp = 3 and Φ = 120).

meridional wind perturbations predicted by the HWM-93 are also in disagreement with the satellite results.

The above results indicate that the HWM-93 does not provide a realistic representation of the average response of middle- and low-latitude *F* region winds to high-latitude disturbances. In the first version of the model, HWM-87 [*Hedin et al.*, 1988], Hedin et al. stated that magnetic activity effects are represented very simplistically. The HWM-87 daytime disturbance winds are in slightly better overall agreement with the WINDII results than those from the HWM-93. This is perhaps a result of additional data added to the model in regions other than the daytime *F* region, coupled with its increased complexity.

The National Center for Atmospheric Research thermosphere-ionosphere electrodynamic general circulation model (TIEGCM) [*Richmond et al.*, 1992] self-consistently calculates the coupled thermosphere-ionosphere parameters, including ion and electron densities, temperatures, velocities, currents, electric potentials, and fields. The inputs to the model include solar heating, auroral inputs, and a lower boundary condition that allows specification of upward propagating tides. The model uses a realistic magnetic field model (International Geomagnetic Reference Field 1985.0). The temporal resolution is 5 min, and the horizontal resolution is 5°. The altitudinal coverage extends from about 100 km to over 500 km, with two grid points per scale height; the height resolution is thus about 25 km in the upper thermosphere. Here we use the TIEGCM version described by *Fesen et al.* [2000].

For comparison with the WINDII results we calculated longitudinally averaged TIEGCM disturbance winds by subtracting geomagnetically quiet (Kp = 2) runs from disturbed (Kp = 4.5) runs, following basically the same procedure used in our data analysis. The original model runs were done for December solstice, March equinox, and June solstice and for solar flux indices of 100 and 150 (the WINDII database has an average $\Phi \cong 125$). These model calculations were made until diurnally reproducible solutions were obtained, which requires about 3 model days. The disturbance winds, given at 5° latitude intervals and hourly universal times, were initially averaged over the 220-280 km height range, transformed to local time-longitude coordinates, and averaged over longitude and solar flux.

Figure 8 presents the WINDII and TIEGCM seasonal disturbance wind vectors as a function of local time and latitude for ΔKp = 2.5. The WINDII perturbation winds for June solstice are less accurate than for the other seasons since the number of measurements during June and July is relativ small (see Figure 1). The WINDII and TIEGCM vector win patterns do not change much with season and show a high degree of hemispheric symmetry. Figure 8 again shows largest WINDII disturbance winds at upper midlatitudes. These are predominantly equatorward in the morning and westward in the late afternoon periods. At low latitudes the WINDII eastward perturbations are largest during morning equinoctial periods. The TIEGCM meridional disturbance winds have very small values in the morning, except at upper midlatitudes, where they are predominantly poleward, in disagreement with the WINDII results. In the afternoon sector the TIEGCM perturbations are predominantly westward at all latitudes. The afternoon meridional disturbances indicate a winter-to-summer flow during the solstices, which is consistent with the results from WINDII.

The local time variations of the WINDII and TIEGCM perturbation winds for each season are presented in more detail in Figure 9. The upper midlatitude zonal wind patterns from

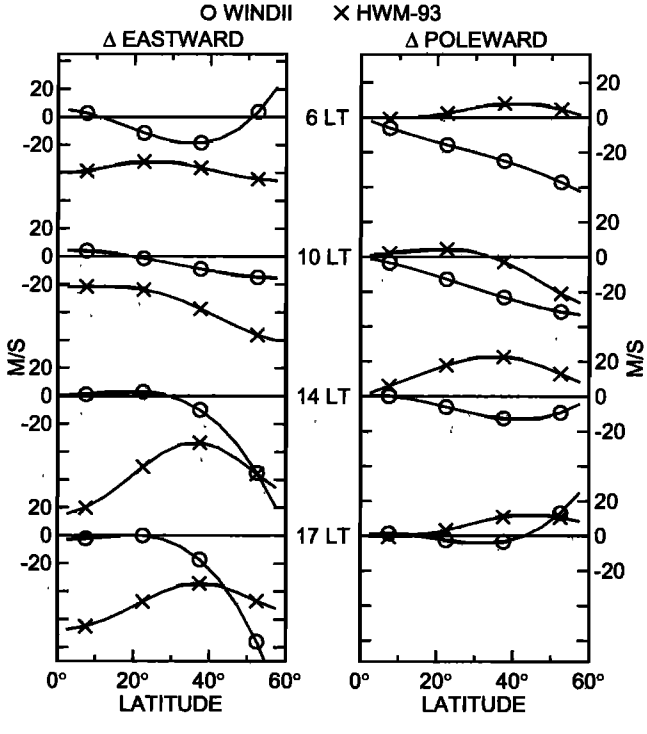

Figure 7. Latitude plots of middle- and low-latitude WINDII (open circles) and HWM-93 (crosses) seasonally and longitudinally averaged disturbance winds (ΔKp = 3 and Φ = 120): (left) change eastward and (right) change poleward.

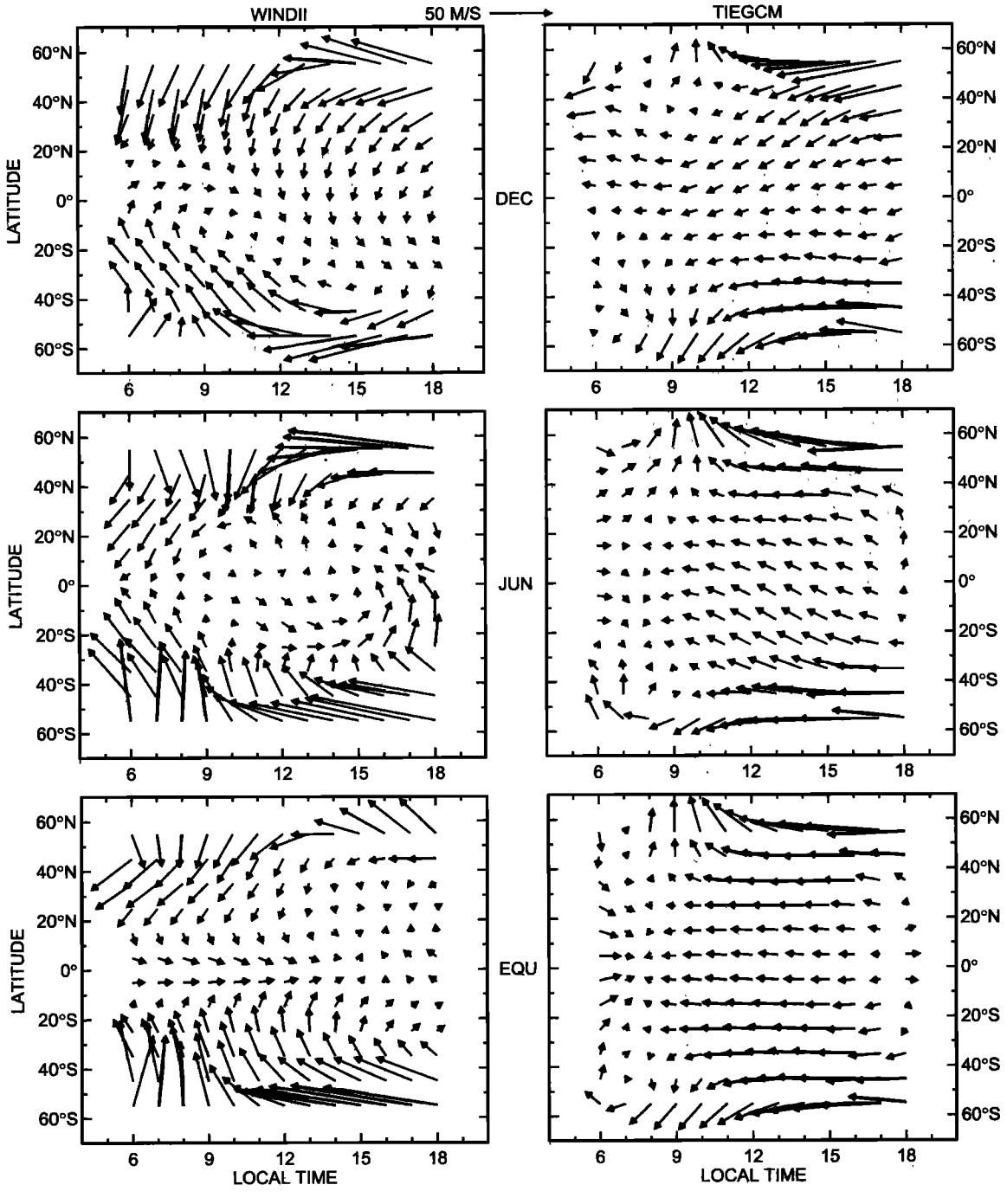

Figure 8. (left) WINDII and (right) TIEGCM longitudinally averaged vector disturbance winds for $\Delta Kp = 2.5$ and $(\Phi) = 120$.

WINDII and TIEGCM show similar local time dependence, with westward perturbations increasing with local time. In the afternoon sector the TIEGCM and satellite disturbance winds decrease noticeably between 55° and 35°. At low latitudes the TIEGCM predicts moderate (about 10 m s^{-1}) westward perturbations, whereas the empirical model has smaller eastward perturbations lasting until midafternoon. There are also significant differences in the meridional components from 35° to 55° up to about 1400 LT, where the satellite data show large equatorward perturbations and the TIEGCM shows mostly poleward disturbances. At lower latitudes both models have small perturbation winds.

We have seen that there are significant discrepancies between the results from WINDII and TIEGCM. It is important to note, however, that there are at least two reasons for the disagreement between average perturbations winds derived from statistical and time-dependent convection models. The first is the likely difference of their average storm times (i.e., times after the onset of storms). Climatological disturbance winds from time-dependent models like the TIEGCM correspond to prolonged stationary disturbed conditions, whereas statistical winds represent averages from a variety of storms, most of them relatively short-lived (less than about 10 hours). Since meridional disturbance winds are strongly

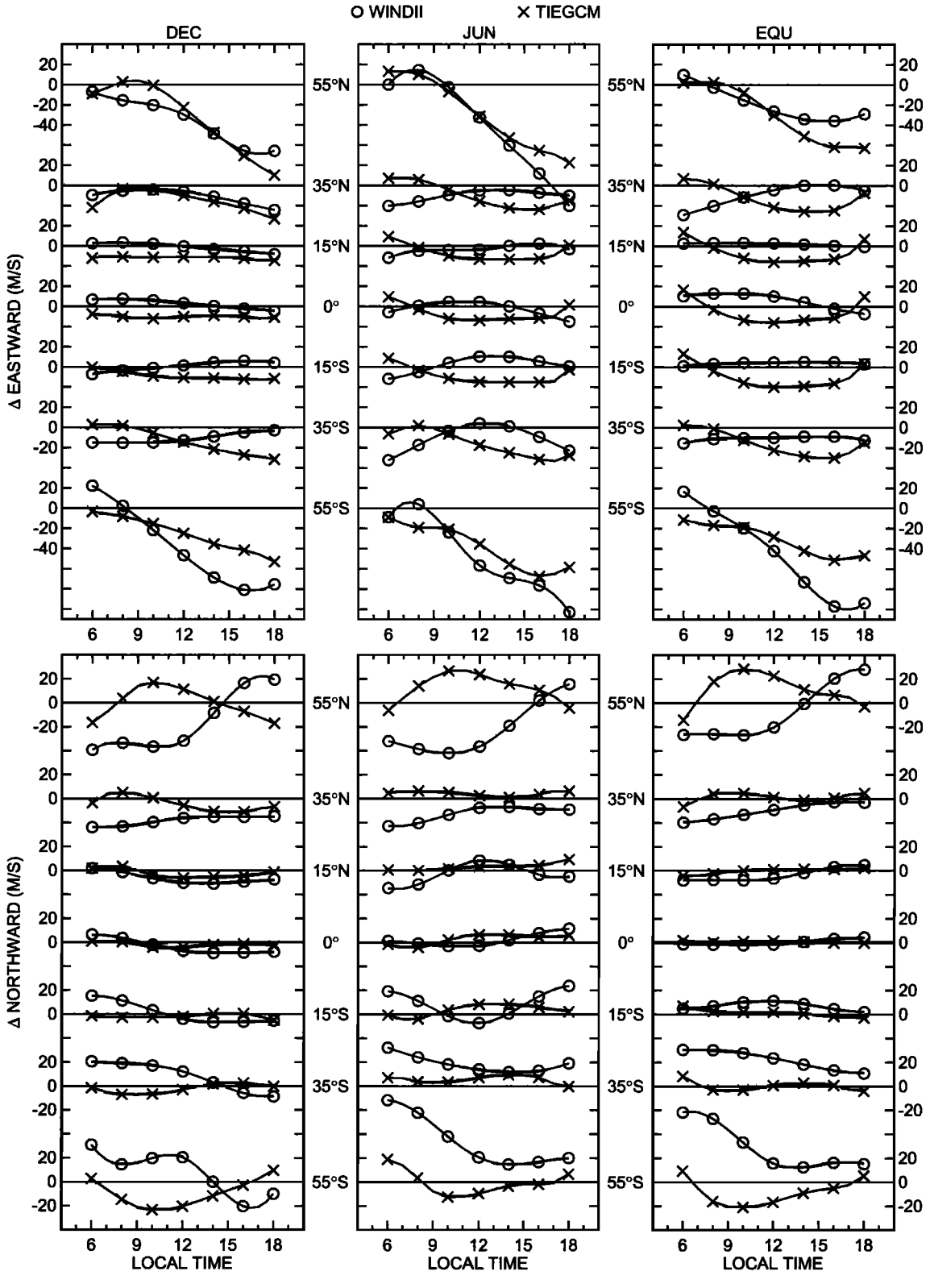

Figure 9. Local time plots of the middle- and low-latitude WINDII (open circles) and TIEGCM (crosses) longitudinally averaged disturbance winds for $\Delta Kp = 2.5$ and $(\Phi) = 120$: (left) December solstice, (middle) June solstice, and (right) combined equinoxes.

time-dependent [*Roble et al.*, 1987; *Burns et al.*, 1995; *Fuller-Rowell et al.*, 1994], different average storm times can result in different climatologies. The second possible reason for the observed disagreements is that general circulation models tend to underestimate the high-latitude Joule heating since they neglect electric field variability as an energy source [*Codrescu et al.*, 1995]. For a Gaussian distribution of small-scale electric field variability around the mean the Joule heating

contribution from the variability is equal to that from the average electric field [*Codrescu et al.*, 2000]. In the TIEGCM runs used in this study the Joule heating and hemispheric power terms [e.g., *Foster et al.*, 1989] were increased by factors of 1.5 and 3, respectively, in an attempt to compensate for this effect by producing more heating. Our results suggest that this increase was not enough to account for the larger observed perturbation winds.

5. Summary

We studied the morphology of the daytime middle- and low-latitude *F* region disturbance winds measured by the WINDII instrument on UARS. We derived a database of perturbation winds by subtracting from the disturbed wind data the corresponding quiet time average values obtained under similar geophysical, orbital, and observing conditions. This methodology removes most of the instrumental and measurement bias from the disturbance wind residuals. The perturbation winds are largely height-independent above 150 km. We used this database to determine the average response of the local time-, latitude-, season-, and solar cycle-dependent perturbation winds to magnetic activity, as measured by the *Kp* index.

The latitudinal profiles of the daytime disturbance winds are nearly identical in the Northern and Southern Hemispheres. The seasonal dependence is also small and is largely restricted to the early morning period for the zonal component and to the afternoon hours for the meridional component. The zonal perturbation winds are mostly westward, except in the early morning sector, where they are eastward at equatorial and upper midlatitudes. The westward disturbance winds increase with latitude and have largest values in the late afternoon sector. The meridional disturbances are mostly equatorward, increase linearly with latitude, and decrease from morning to early afternoon. The upper midlatitude meridional perturbations become poleward in the late afternoon sector. The zonal and meridional perturbations increase roughly linearly with *Kp*. In the late afternoon sector the zonal disturbance winds also expand to lower latitudes with increasing magnetic activity. The zonal perturbation winds do not change much with solar flux, but the equatorward winds increase with decreasing decimetric solar flux. The zonal and meridional perturbations exhibit a complex longitudinal dependence.

We developed empirical analytical models of longitudinally averaged WINDII disturbance winds as a function of local time, latitude, season, and magnetic activity. For the meridional component we have also added a simple solar flux correction term. The WINDII disturbances are in poor agreement with the predictions from the HWM-93 at essentially all local times. There are also noticeable differences between the WINDII and the TIEGCM average perturbation winds, particularly in the morning sector, where the TIEGCM predicts mostly very weak equatorward winds. The latter discrepancies are partly due to high-latitude electric field variability, which is not fully accounted for in the TIEGCM, and perhaps also to the different average storm times.

Acknowledgments. The work at Utah State was supported by NASA through grant NAGW-4469. C. G. F. was supported by NSF/CEDAR grant ATM 9796035 and NASA grant 5-3598. The WINDII project is supported by the Canadian Space Agency and the Centre d'Etudes Spatiales of France. Support for scientific data analysis was provided by the Natural Sciences and Engineering Research Council of Canada.

Janet G. Luhmann thanks Seiji Kawamura and another referee for their assistance in evaluating this paper.

References

Buonsanto, M. J., Millstone Hill incoherent scatter *F* region observations during the disturbances of June 1991, *J. Geophys. Res.*, *100*, 5743-5755, 1995.

Buonsanto, M. J., and O. G. Witasse, An updated climatology of thermospheric winds and *F* region ion drifts over Millstone Hill, *J. Geophys. Res.*, *104*, 24,675-24,687, 1999.

Burns, A. G., T. L. Killeen, W. Deng, G. R. Carignan, and R. G. Roble, Geomagnetic storm effects in the low- to middle-latitude upper thermosphere, *J. Geophys. Res.*, *100*, 14,673-14,692, 1995.

Codrescu, M. V., T. J. Fuller-Rowell, and J. C. Foster, On the importance of *E*-field variability for the Joule heating in the high-latitude thermosphere, *Geophys. Res. Lett.*, *22*, 2393-2396, 1995.

Codrescu, M. V., T. J. Fuller-Rowell, J. C. Foster, J. M. Holt, and S. J. Cariglia, Electric field variability associated with the Millstone Hill electric field model, *J. Geophys. Res.*, *105*, 5265-5273, 2000.

Crowley, G., B. A. Emery, R. G. Roble, H. C. Carlson, and D. J. Knipp, Thermospheric dynamics during September 18-19, 1984, 2, Validation of the NCAR thermospheric general circulation model, *J. Geophys. Res.*, *94*, 16945-16959, 1989.

Duboin, M. L., and M. Lafeuille, Thermospheric dynamics above Saint-Santin: Statistical study of the data set, *J. Geophys. Res.*, *97*, 8661-8671, 1992.

Emery, B. A., et al., AMIE-TIGCM comparisons with global ionospheric and thermopsheric observations during the GEM/SUNDIAL period of March 28-29, 1992, *J. Geophys. Res.*, *101*, 26,681-26,696, 1996.

Emmert, J. T., Climatology of upper thermospheric daytime neutral winds from satellite observations, Ph.D. dissertation, 146 pp., Utah State Univ., Logan, 2001.

Fejer, B. G., and L. Scherliess, Time-dependent response of equatorial ionospheric electric fields to magnetospheric disturbances, *Geophys. Res. Lett.*, *22*, 851-854, 1995.

Fejer, B. G., and L. Scherliess, Empirical models of storm time equatorial zonal electric fields, *J. Geophys. Res.*, *102*, 24,047-24,056, 1997.

Fejer, B. G., J. T. Emmert, G. G. Shepherd, and B. H. Solheim, Average daytime *F* region disturbance neutral winds measured by UARS: Initial results, *Geophys. Res. Lett.*, *27*, 1859-1862, 2000.

Fesen, C. G., A. D. Richmond, and R. G. Roble, Theoretical effects of geomagnetic activity on thermospheric tides, *J. Geophys. Res.*, *98*, 15,599-15,612, 1993.

Fesen, C. G., R. G. Roble, and M.-L. Duboin, Simulations of seasonal and geomagnetic activity effects at Saint Santin, *J. Geophys. Res.*, *100*, 21,397-21,407, 1995.

Fesen, C. G., G. Crowley, R. G. Roble, A. D. Richmond, and B. G. Fejer, Simulation of the pre-reversal enhancement in the low latitude vertical ion drifts, *Geophys. Res. Lett.*, *27*, 1851-1854, 2000.

Foster, J. C., T. Fuller-Rowell, and D. S. Evans, Quantitative patterns of large-scale field-aligned currents in the auroral ionosphere, *J. Geophys. Res.*, *94*, 2555-2564, 1989.

Fujiwara, H., S. Maeda, H. Fukunishi, T. J. Fuller-Rowell, and D. S. Evans, Global variations of thermospheric winds and temperatures caused by substorm energy injection, *J. Geophys. Res.*, *101*, 225-240, 1996.

Fuller-Rowell, T. J., M. V. Codrescu, R. J. Moffet, and S. Quegan, Response of the thermosphere and ionosphere to geomagnetic storms, *J. Geophys. Res.*, *99*, 3893-3914, 1994.

Fuller-Rowell, T. J., M. V. Codrescu, H. Rishbeth, R. J. Moffet, and S. Quegan, On the seasonal response of the ionosphere and thermosphere to geomagnetic storms, *J. Geophys. Res.*, *101*, 2343-2354, 1996.

Gussenhoven, M. S., D. A. Hardy, and N. Heinemann, Systematics of the equatorward diffuse auroral boundary, *J. Geophys. Res.*, *88*, 5692-5708, 1983.

Hagan, M. E., Quiet time upper thermospheric winds over Millstone Hill between 1984 and 1990, *J. Geophys. Res.*, *98*, 3731-3739, 1993.

Hedin, A. E., MSIS-86 thermospheric model, *J. Geophys. Res.*, *92*, 4649-4662, 1987.

Hedin, A. E., N. W. Spencer, and T. L. Killeen, Empirical global model of upper thermosphere winds based on Atmospheric and Dynamics Explorer satellite data, *J. Geophys. Res.*, *93*, 9959-9978, 1988.

Hedin, A. E., et al., Revised global model of upper thermosphere winds using satellite and ground-based observations, *J. Geophys. Res., 96,* 7657-7688, 1991.

Hedin, A. E., et al., Empirical wind model for the upper, middle, and lower atmosphere, *J. Atmos. Terr. Phys., 58,* 1421-1447, 1996.

Hernandez, G., Middle-latitude thermospheric neutral kinetic temperatures, 1, Solar, geomagnetic, and long-term effects, *J. Geophys. Res., 87,* 1623-1632, 1982.

Hernandez, G., R. G. Roble, and J. H. Allen, Midlatitude thermospheric winds and temperatures and their reaction to the auroral electrojet activity indices, *Geophys. Res. Lett., 7,* 677-680, 1980.

Kawamura, S., Y. Otsuka, S.-R. Zhang, S. Fukao, and W. L. Oliver, A climatology of middle and upper atmosphere radar observations of thermospheric winds, *J. Geophys. Res., 105,* 12,777-12,788, 2000.

Miller, K. L., M. Lemon, and P. G. Richards, A meridional wind climatology from a fast model for the derivation of meridional winds from the height of the ionospheric *F2* region, *J. Atmos. Terr. Phys., 59,* 1805-1822, 1997.

Miller, N. J., L. H. Brace, N. W. Spencer, and G. R. Carignan, DE 2 observations of disturbances in the upper atmosphere during a geomagnetic storm, *J. Geophys. Res., 95,* 21,017-21,031, 1990.

Reber, C. A., C. E. Trevathan, R. J. McNeal, and M. R. Luther, The Upper Atmosphere Research Satellite (UARS) mission, *J. Geophys. Res., 98,* 10,643-10,647, 1993.

Reddy, C. A., and H. G. Mayr, Storm-time penetration to low latitudes of magnetospheric-ionospheric convection and convection-driven thermospheric winds, *Geophys. Res. Lett., 25,* 3075-3073, 1998.

Richmond, A. D., E. C. Ridley, and R. G. Roble, A thermosphere-ionosphere general circulation model with coupled electrodynamics, *Geophys. Res. Lett., 19,* 601-604, 1992.

Roble, R. G., J. M. Forbes, and F. A. Marcos, Thermospheric dynamics during the March 22, 1979 magnetic storm, 1, Model simulations, *J. Geophys. Res., 92,* 6045-6068, 1987.

Shepherd, G. G., et al., WINDII, the Wind Imaging Interferometer on the Upper Atmosphere Research Satellite, *J. Geophys. Res., 98,* 10,725-10,750, 1993.

Titheridge, J. E., Winds in the ionosphere: A review, *J. Atmos. Solar Terr. Phys., 57,* 1681-1714, 1995.

Zhang, S. P., and G. G. Shepherd, Neutral winds in the lower thermosphere observed by WINDII during April 4-5th, 1993 storm, *Geophys. Res. Lett., 27,* 1855-1858, 2000.

J. T. Emmert, and B. G. Fejer, Center for Atmospheric and Space Sciences, Utah State University, Logan, UT 84322-4405. (bfejer@cc.usu.edu)

C. G. Fesen, W. B. Hanson Center for Space Sciences, University of Texas at Dallas, Richardson, TX 75083-0688.

G. G. Shepherd and B. H. Solheim, Centre for Research in Earth and Space Science, York University, Toronto, Ontario, Canada M3J 1P3.

(Received September 26, 2000; revised January 30, 2001;
accepted January 30, 2001.)